Full length article

Designing shape-memory-like microstructures in intercalation materials

Delin Zhang [a], Ananya Renuka Balakrishna [a,b,*]

[a] *Department of Aerospace and Mechanical Engineering, University of Southern California, Los Angeles, 90089, CA, USA*
[b] *Materials Department, University of California Santa Barbara, Santa Barbara, 93106, CA, USA*

ARTICLE INFO

ABSTRACT

During the reversible insertion of ions, lattices in intercalation materials undergo structural transformations. These lattice transformations generate misfit strains and volume changes that, in turn, contribute to the structural decay of intercalation materials and limit their reversible cycling. In this paper, we draw on insights from shape-memory alloys, another class of phase transformation materials, that also undergo large lattice transformations but do so with negligible macroscopic volume changes and internal stresses. We develop a theoretical framework to predict structural transformations in intercalation compounds and identify crystallographic design rules necessary for forming shape-memory-like microstructures in intercalation materials. We use our approach to systematically screen open-source structural databases comprising $n > 5000$ pairs of intercalation compounds. We identify candidate compounds, such as $Li_xMn_2O_4$ (Spinel), $Li_xTi_2(PO_4)_3$ (NASICON), that approximately satisfy the crystallographic design rules and can be precisely doped to form shape-memory-like microstructures. Throughout, we compare our analytical results with experimental measurements of intercalation compounds. We find a direct correlation between structural transformations, microstructures, and increased capacity retention in these materials. These results, more generally, show that crystallographic designing of intercalation materials could be a novel route to discovering compounds that do not decay with continuous usage.

1. Introduction

Intercalation is the reversible insertion of guest species (e.g., molecules, atoms, or ions) into a material's lattice structure, see Fig. 1(a). This reversible insertion makes intercalation materials well-suited for sustainable energy storage, such as graphite in hydrogen storage, electrodes in lithium batteries, and chalcogenides in electrochromic applications [1–7]. This intercalation, however, is typically accompanied by an abrupt structural transformation of the material that shortens its lifespan.

At the microscopic scale, this intercalation-induced transformation leads to a misfit between neighboring lattices which, in turn, leads to a stressed interface. At the macroscopic scale, this transformation induces volume changes of the intercalation material [8] and leads to non-uniform intercalation behavior [9]. These unwanted features can nucleate microcracks [10], see Fig. 1(b); result in mechanically damaged surfaces (delamination), see Fig. 1(c) [11,12]; and, in extreme cases, lead to the amorphization of the intercalation material [13,14]. The structural transformation and its accompanying coherency stress thus contribute to the decay of intercalation materials, which need to be replaced eventually [15,16]. However, common applications such as lithium batteries require these materials to survive thousands of intercalation cycles.

In shape memory alloys (SMAs), another class of phase transformation materials, the structural changes of lattices are also accompanied by large strains. Despite the large transformation strains, SMAs form characteristic microstructures with small coherency stresses (austenite–martensite interface), negligible volume changes (self-accommodating), and low fatigue ($\lambda_2 = 1$). In these materials, lattices of different orientations rotate and/or shear to fit with each other resulting in the formation of twin boundaries, see Fig. 2(a) [17]. These finely twinned microstructures minimize coherency stresses at the phase boundary, and, for specific geometric conditions, adapt to the macroscopic material shape. These microstructures, if stabilized in intercalation electrodes, could mitigate the chemo-mechanical challenges plaguing solid-state battery materials.

Intercalation materials and SMAs share several similarities. First, during phase transformation, lattices in both materials undergo reversible structural changes at a critical point. For example, intercalation electrodes transform between the intercalated (lithiated) and reference (delithiated) phases at critical intercalant (guest-species such as Li) concentrations, while SMAs transform between the austenite and martensite phases at the transformation temperature, see Fig. 2.

* Corresponding author.
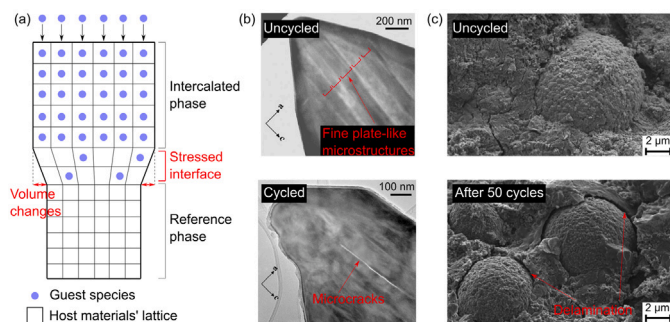 *E-mail address:* ananyarb@ucsb.edu (A. Renuka Balakrishna).

Fig. 1. (a) Schematic illustration of intercalation during which guest species are reversibly inserted into a material's lattice structure. This insertion induces structural transformation of the material resulting in stressed interfaces and volume changes. On repeated intercalation, (b) the material's stressed interfaces nucleate microcracks [10] (Reprinted with permission from Electrochemical Society and Institute of Electrical and Electronics Engineers) and (c) its volume changes lead to delamination [11]. These chemo-mechanical degradations eventually lead to a decay in material performance.
Source: Reprinted with permission from American Chemical Society.

Fig. 2. Phase transformation microstructures in intercalation materials bear a striking resemblance to microstructures in shape memory alloys. (a) An austenite–martensite interface showing finely twinned domains in the Cu-14.0%Al-3.9%Ni shape-memory alloy. Image courtesy of Chu and James [17]. (b) A bright field image of a partially transformed $Li_xMn_2O_4$ showing finely twinned domains.
Source: Reproduced with permission from American Chemical Society [18].

Second, during phase transformations, atoms of the host intercalation material and atoms of the SMA undergo cooperative and homogeneous displacements. For example, an intercalation material's lattices undergo structural changes during Li-diffusion, which is analogous to the SMA's lattices undergoing structural changes during thermal diffusion [18,19]. Besides these similarities, researchers have shown evidence of intercalation materials that have near-zero volume changes despite changes to their lattice geometry [20]: the Na-ion cathode $Na_{1.0}Li_{0.2}Ni_{0.25}Mn_{0.75}O_\delta$ on intercalation has a near-zero volume change despite undergoing $\sim 1\%$ anisotropic linear strains. This example is analogous to the volume-preserving transformations observed in shape-memory alloys [21]. Other examples include the recent discoveries of zero-strain intercalation electrodes [22], a series of spinel compounds with $< 0.2\%$ volume change [23], and the Mo-doped V_2O_5, which have reduced coherency stresses during first-order phase transformations [24].

The structural changes in the host intercalation material are supported by, in-situ, X-ray diffraction experiments that show abrupt lattice transformations. Recently, researchers imaged a nanotwinned microstructure in a Spinel cathode ($Li_xMn_2O_4$) that forms during electrochemical lithiation, see Fig. 2(b) [18]. These nanotwinned microstructures resemble the austenite–martensite interface in SMAs and are formed to relieve coherency stresses at the phase boundary. In another study, researchers showed that ordered microstructures with plate-like features form in $LiFePO_4$ electrodes to lower stresses in the particle geometry [10]. While these elementary features of twinned microstructures have been observed in some intercalation materials, shape-memory-like microstructures with self-accommodating or low-fatigue characteristics have not.

The self-accommodating and low-fatigue ($\lambda_2 = 1$) microstructures have important advantages that could address the chemo-mechanical challenges in intercalation materials. The self-accommodation microstructure, adapts to the original shape of the material without any macroscopic change in volume, despite significant structural changes at the atomic scale [25]. These microstructures would particularly benefit solid-state architectures in which repeated volume changes of the intercalation electrode leads to electrode/ electrolyte delamination [11,26] and/or fracture [27]. The $\lambda_2 = 1$ microstructure corresponds to an exactly compatible and stress-free phase boundary that can move back and forth in the material, reversibly, several thousand times, and yet induce ultra-low fatigue [28,29]. This exactly compatible interface would minimize internal stress accumulations in an intercalation electrode and mitigate failure arising from microcracking [30]. These microstructures are observed in shape-memory alloys
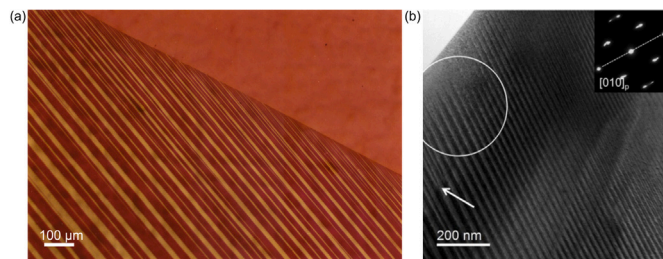
and other functional materials and have contributed to a phenomenal improvement in their performance [31].

The self-accommodating or $\lambda_2 = 1$ microstructures form when the material's lattice parameters satisfy particular geometric relationships [32], and when unit cells deform along specific structural transformation pathways [33]. The lattice geometries of several intercalation materials are determined for the reference and intercalated phases, however, the structural transformation pathways are dependent on how unit cells are categorized into different crystal symmetries and space groups.[1] This ambiguity could result in multiple solutions for the structural transformation pathways and it is important to identify these deformations to predict the microstructural patterns at the continuum length scale.

The central aim of this work is to quantify structural transformations in commonly used intercalation materials and to identify the crystallographic design rules necessary to reduce coherency stresses and volume changes for intercalation materials. We hypothesize that although some intercalation materials *approximately* satisfy these lattice parameter conditions, most of the intercalation compounds do not satisfy the crystallographic geometric constraints necessary to form the special microstructures with chemo-mechanical advantages. Additionally, we hypothesize that intercalation materials approximately satisfying the geometric constraints – under similar electrochemical operating conditions – show improved material performance (e.g., reversible cycling and capacity retention). In this paper, we test these hypotheses by conducting a systematic search of the structural data of intercalation materials and analyzing microstructures that form in these materials during phase transformation.

This paper is organized as follows: In the Methods section, we outline our theoretical framework to quantify structural transformation pathways and identify the crystallographic design rules necessary to form shape-memory-like microstructures in intercalation materials. In the Results section, we use our theoretical framework for two studies: In Study 1, we analyze the structural transformations in commonly used crystal structures (e.g., Layered, Spinel, Olivine) and identify families of intercalation compounds that are capable of forming shape-memory-like microstructures. In Study 2, we apply our algorithms to the Materials Project database to analyze whether any known intercalation compound can form shape-memory-like microstructures during phase transformation. Our results show that none of the existing intercalation compounds exactly satisfy the geometric constraint

---

[1] For example, the $Li_xMn_2O_4$ ($1 \leq x \leq 2$) can be described using both a conventional tetragonal unit cell ($F4_1/ddm$, $a = 8.0$ Å, $c = 9.3$ Å) and a primitive tetragonal unit cell ($I4_1/amd$, $a = 5.7$ Å, $c = 9.3$ Å) [34], however, the measured volume changes correspond to that of a conventional unit cell in the reference state. Similarly, Melot et al. use the $Fe_2(MoO_4)_3$ reference unit cell to identify all potential symmetry-lowering transformation pathways [35].
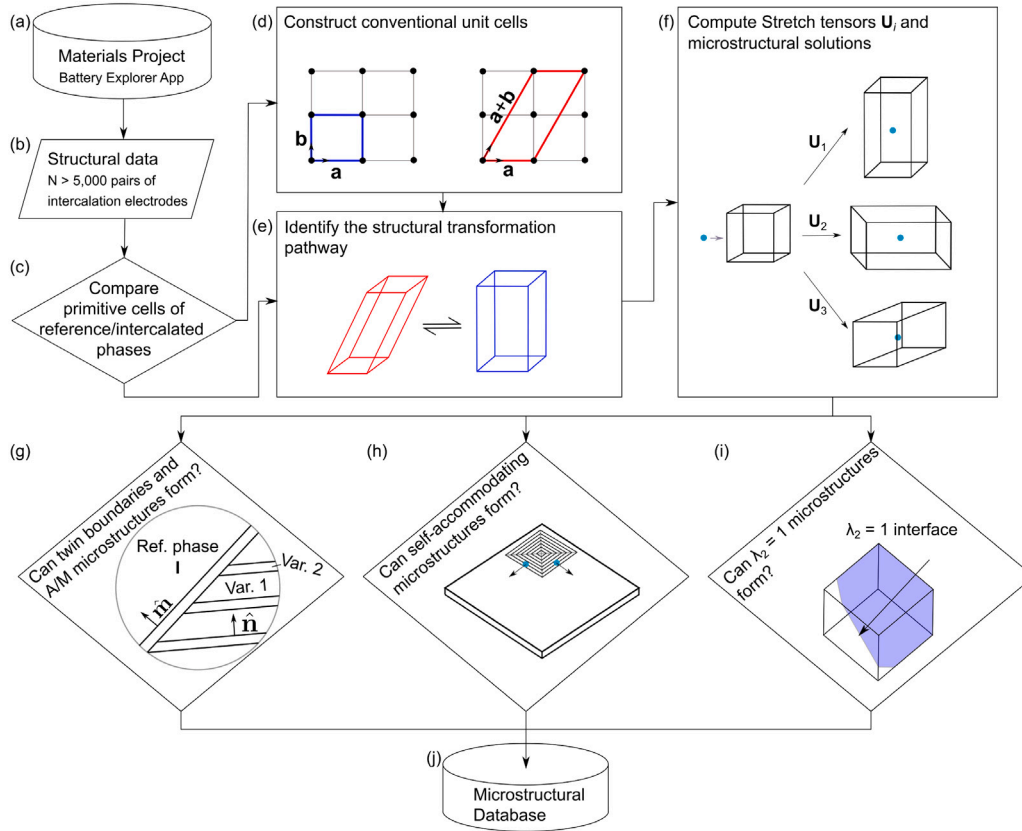
Fig. 3. Workflow steps of our theoretical framework. (a–b) We first extract structural data of over 5000 pairs of intercalation compounds from the Materials Project database. We then apply our developed structural transformation algorithm (c–d) to determine unit cells in the reference and intercalated phases, and (e–f) construct the optimal stretch tensor to describe the transformation pathway. Finally, we use the computed stretch tensor for each compound to identify potential candidates that can form (g) twin boundaries, austenite/martensite (A/M), (h) self-accommodating, or (i) highly reversible microstructures. (j) The solutions of these compounds are stored in the microstructural database.

for self-accommodating or highly reversible microstructures; however, intercalation compound groups, such as the Spinels, Tavorites, Phosphates, and NASICON, satisfy a few of the crystallographic design principles. These compounds can be systematically doped either using first-principles calculations or site-selective synthesis to precisely satisfy lattice parameter relationships [24,36–38]. Throughout, we compare our analytical results with experimental observations and show a direct correlation between structural transformations, microstructural patterns, and capacity retention. Our results, more broadly, quantify the structural transformation pathways for over $n > 5000$ pairs of intercalation compounds and identify the crystallographic design rules necessary to mitigate chemo-mechanical challenges in intercalation materials.

2. Crystallographic design principles

In this section, we outline the theoretical framework that we use to compute the structural transformation of unit cells during intercalation and to analyze how these transformations collectively generate microstructures at the continuum scale, see Fig. 3. Before we outline our framework, we describe a Cauchy-Born rule that is central to our analysis: The Cauchy-Born rule is a basic hypothesis used in the mathematical formulation of solid mechanics which relates the deformation of the bulk solid to the movement of atoms in a crystal [39]. This rule gives an exact correspondence between the continuum microstructures at a material point and the structural transformations of individual lattices. This Cauchy-Born rule allows us to impose special lattice geometries as a necessary condition for characteristic microstructures (e.g., austenite–martensite, self-accommodating, $\lambda_2 = 1$) to form during phase transformations. We use the Cauchy-Born rule in our framework and identify the geometric constraints necessary to form shape-memory-like microstructures in intercalation compounds.

2.1. Structural transformation

Structural transformations in intercalation materials are triggered by ion insertion/extraction that is accompanied by redox reactions. The resulting difference between reference and intercalated phases eventually manifests in X-ray measurements of structure and lattice parameters. We use this information to investigate the structural transformation of unit cells in intercalation compounds and describe it using a stretch tensor $\mathbf{U}$.[2] This stretch tensor maps a unit cell in the reference phase (i.e., before intercalation) to the corresponding unit cell in the intercalated phase (i.e., after intercalation). This stretch tensor, for a given compound, is not unique and can have multiple solutions based on how we choose the unit cells for reference and intercalated phases, see Fig. 4. In this section, we describe our algorithm that determines an optimal stretch tensor for a given intercalation compound. We use these optimal stretch tensors to predict microstructural patterns at the continuum scale.

Fig. 4 shows a schematic illustration of a unit cell in the reference phase, which is described using three linearly independent lattice vectors $\mathbf{E}_R = \{\mathbf{e}_{R1}, \mathbf{e}_{R2}, \mathbf{e}_{R3}\}$. These lattice vectors enclose the smallest repeatable volume and constitute a primitive unit cell. On transformation the materials undergo a structural change and a unit cell is now described by lattice vectors $\mathbf{E}_I = \{\mathbf{e}_{I1}, \mathbf{e}_{I2}, \mathbf{e}_{I3}\}$. However, this definition of a unit cell is not unique as other combinations of lattice vectors describing unit cells $\mathbf{E}_I^A = \{\mathbf{e}_{I1}^A, \mathbf{e}_{I2}^A, \mathbf{e}_{I3}^A\}$ (or $\mathbf{E}_I^B$, or $\mathbf{E}_I^C$) generate the

---

[2] A stretch tensor is a mathematical quantity, i.e., a rank-2 matrix, which provides a linear mapping of unit cells between the reference and intercalation phases. A brief description of mathematical quantities introduced in this paper is provided in Table A.2.
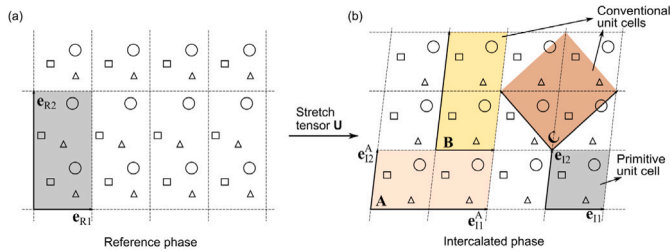
Fig. 4. A schematic illustration of primitive and conventional unit cells in reference and intercalated (or transformed) phases. (a) Vectors $\{\mathbf{e}_{R1}, \mathbf{e}_{R2}\}$ enclose the smallest repeatable unit cell (or the primitive cell) in the reference phase. (b) Vectors $\{\mathbf{e}_{I1}, \mathbf{e}_{I2}\}$ enclose a primitive cell in the intercalated phase. The primitive cell of the reference phase contains twice as many atoms as that of the primitive cell of the intercalated phase. In subfigure (b) we illustrate three representative examples of conventional unit cells–A, B, C–which contain the same number of atoms as the primitive cell of the reference phase. We note that these conventional cells can be described in multiple ways, and thus the stretch tensor $\mathbf{U}$ mapping unit cells between reference and intercalated phases can have more than one solution.

same lattice points in 3D space, see Fig. 4. These latter unit cells, called conventional cells, typically enclose a larger volume (relative to $\mathbf{E}_I$) and can be described in multiple ways. Each conventional cell is related to the primitive unit cell via a lattice correspondence matrix $\mathbf{P} \in \mathbb{Z}^3$ as $\mathbf{E}_I^A = \mathbf{E}_I \mathbf{P}^A$, and several correspondence matrices can exist based on our choice of the conventional cells.[3] Based on our choice of unit cells for the reference and intercalated phases, we would have more than one stretch tensor describing the transformation between the two phases.

Following Refs. [33,40], we propose an algorithm to identify an optimal stretch tensor, from a list of potential stretch tensors, by minimizing the transformation pathways between the reference and intercalated unit cells. We describe this algorithm in detail in the Supplementary Material, and outline the three key steps below:

1. Determine the primitive unit cells of reference and intercalated phases and identify all potential lattice correspondence matrices $\mathbf{P}$ for a given compound. In the Supplementary Material, we outline the specific steps to compute $\mathbf{P}$ using a pair of primitive unit cells as an example.

2. Compute the stretch tensor $\mathbf{U}$ mapping a unit cell of the reference phase to the corresponding unit cell of the intercalated phase. The general form for the mapping is given by $\mathbf{F} \mathbf{E}_R \mathbf{P}_R = \mathbf{E}_I \mathbf{P}_I$ in which $\mathbf{F}$ is the deformation gradient, and the transformation stretch tensor $\mathbf{U}$ is the unique positive-definite square root of $\mathbf{F}^T \mathbf{F}$.[4] This stretch tensor $\mathbf{U}$ is unique for a given pair of correspondence matrices $\mathbf{P}_R, \mathbf{P}_I$, and we determine all possible stretch tensors by cycling through the set of correspondence matrices identified in the first step.

3. Identify an optimal lattice correspondence (and thus the stretch tensor) that minimizes a distance function representing the total strain of a structural transformation: $\mathrm{dist}(\mathbf{P}_R, \mathbf{P}_I, \mathbf{E}_R, \mathbf{E}_I) = \left\| \mathbf{U}^{-2} - \mathbf{I} \right\|^2$. Here, $\|.\|$ is the Frobenius norm, $\|\mathbf{A}\|^2 = \mathbf{A} : \mathbf{A} = \mathrm{Tr}(\mathbf{A}^T \mathbf{A})$. By minimizing this distance function over the set of stretch tensors computed in the second step, we determine the optimal lattice correspondence and the transformation stretch tensor for a given intercalation compound.

Further details of this algorithm using $Li_x Fe_2(MoO_4)_3$ as an example is described in the Supplementary Material. In principle, this algorithm can be applied to determine stretch tensors for any crystalline material undergoing a first-order phase transformation; however, for the present

work, we apply our theoretical framework to intercalation compounds commonly used in batteries. We use the computed optimal stretch tensors in our microstructural analysis—that is, we determine whether an intercalation compound satisfies the crystallographic design principles described in the next section.

2.2. Microstructures

The crystallographic theory of martensites is an energy minimization theory [32] in which the material's energy is described as a function of a lattice deformation gradient $\mathbf{F}$. The lattice deformation gradient at the *atomic* scale penalizes the elastic energy arising from lattice misfit. Minimizing this elastic energy then results in the formation of finely twinned microstructures at the *continuum* scale, see Fig. 2. This theory has been widely used to explain the characteristic microstructures in shape memory alloys, ferroelectrics, ferromagnets, and more recently in light-interactive materials [41–43]. We use this theory to identify the geometric conditions necessary to form shape-memory-like microstructures in intercalation materials.

Following the crystallographic theory of martensites, we next list the criteria necessary to form the four candidate shape-memory-like microstructures in Table 1. These criteria identify specific lattice geometries quantified by stretch tensors $\mathbf{U}$ that are necessary to form twins, austenite/martensite, self-accommodating, and $\lambda_2 = 1$ (stress-free) microstructures. We identify these microstructures having several advantages that, if stabilized in intercalation materials, would help mitigate their chemo-mechanical degradation:

1. Shape-memory-like microstructures, such as the twins and austenite/martensite microstructure, reduce the elastic energy arising from misfit strains between neighboring lattices and across phase boundaries, respectively. This reduced energy suppresses microcracking of intercalation materials with repeated usage.

2. The self-accommodation microstructure, adapts to the original shape of the material without any macroscopic change in volume, despite significant structural changes at the atomic scale. These microstructures have the potential to eliminate large volume changes of intercalation electrodes, which in turn lead to delamination in the composite electrode/electrolyte system.

3. The $\lambda_2 = 1$ microstructure corresponds to an exactly compatible and stress-free phase boundary that separates the reference phase from the intercalated phase. This phase boundary is a coherent, unstretched, and consequently unstressed planar interface. This interface eliminates interfacial stresses that commonly arise during phase transformations, and has contributed to a phenomenal improvement in the reversible cycling of phase transformation materials. For example, in Ti-Ni-Cu shape-memory alloys, another material, the $\lambda_2 = 1$ microstructures have enhanced its reversible phase transformation cycles over ten million times with ultra-low fatigue [31]. We provide a detailed perspective on these microstructures in the Supplementary Material.

3. Results

In Study 1, we apply our theoretical framework to commonly used cathode compounds (see Fig. 5(a)), and compare our analysis with microstructural measurements of $Li_x Mn_2 O_4$ and X-ray diffraction measurements for $n = 25$ intercalation compounds. In Study 2, we apply our framework to a larger structural database of intercalation compounds (i.e., Materials Project database comprising structural data for over 5158 pairs of reference/intercalated compounds).[5] We systematically

---

[3] Similarly, the unit cells in the reference phase can be described in multiple ways.

[4] Please see Table A.2 for the physical meaning of a deformation gradient.

---

[5] Intercalation compounds such as $Li_x V_2 O_5$ undergo multiple phase transformations as a function of Li-content. In these cases, we categorize the end products across each phase transformation stage as a distinct pair of intercalation compounds.

Table 1

Crystallographic design principles to form twin interfaces, austenite/martensite microstructures, self-accommodating, and $\lambda_2 = 1$ microstructures in intercalation materials. The stretch tensors describing the lattice transformation must satisfy specific geometric conditions to form shape-memory-like microstructures. Further details on the notations used here are listed in Table A.1.

Microstructure	Geometric condition	Notation	Advantages
Twin	$\mathbf{QU}_I - \mathbf{U}_J = \mathbf{a} \otimes \hat{\mathbf{n}}$	Stretch tensors $\mathbf{U}_I$, $\mathbf{U}_J$ Rotation matrix $\mathbf{Q}$ Vectors $\mathbf{a} \neq 0$, $\hat{\mathbf{n}}$	Exactly compatible interface
Austenite/Martensite	$\mathbf{Q}'(f\mathbf{QU}_J + (1-f)\mathbf{U}_I)$ $= \mathbf{I} + \mathbf{b} \otimes \hat{\mathbf{m}}$	Rotation matrices $\mathbf{Q}'$, $\mathbf{Q}$ Volume fraction f Identity matrix $\mathbf{I}$ Vectors $\mathbf{b} \neq 0$, $\hat{\mathbf{m}}$	Energy minimizing deformation
Self-accommodating[a]	$\det\mathbf{U} = 1$ No relative stretch along c-axis	Stretch tensor $\mathbf{U}$	No macroscopic change in shape and volume
$\lambda_2 = 1$	$\mathbf{QU}_I - \mathbf{I} = \mathbf{b} \otimes \hat{\mathbf{m}}$	Rotation matrix $\mathbf{Q}$ Vectors $\mathbf{b} \neq 0$, $\hat{\mathbf{m}}$	Highly-reversible transformation

[a]The listed self-accommodation condition applies to all Bravais lattice symmetries except the monoclinic symmetry in the reference phase. For these cases, we use $\det\mathbf{M} = 1$ and further details are described in Supplementary Material.
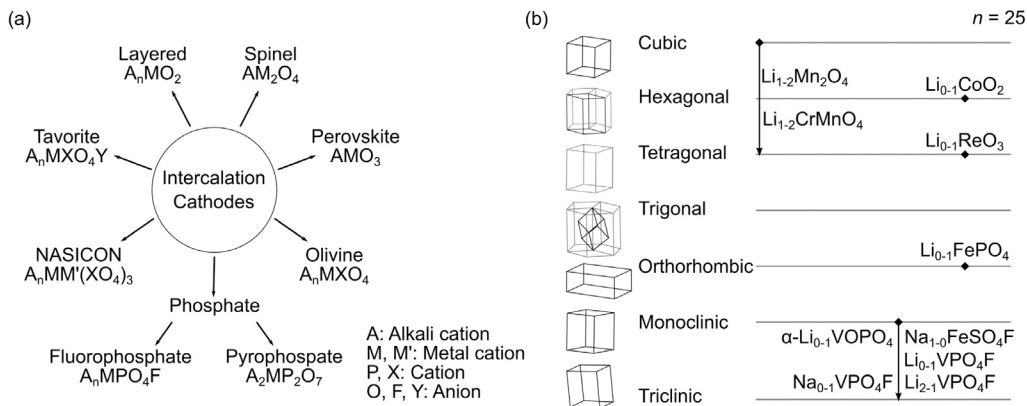

Fig. 5. (a) Crystal structures of commonly used intercalation cathodes in lithium batteries. We extract structural data of intercalation cathodes ($n = 25$) from these families in Study 1. (b) Our analysis shows that only 7 out of 25 intercalation compounds show a change in lattice symmetry during phase transformation.

search and analyze this database to determine whether any known intercalation compound satisfies the crystallographic design principles identified in Table 1. Our findings show that Spinels, Tavorites, Phosphates, and NASICON, are a group of intercalation compounds that approximately satisfy the fundamental design principles necessary to form crystallographic microstructures. We identify specific candidate compounds that approximately satisfy the geometric conditions in Table 1 for forming $\lambda_2 = 1$ and/or self-accommodation microstructures, which could be systematically doped to precisely satisfy the geometric constraints described in Table 1.

3.1. Study 1

We compute the stretch tensors $\mathbf{U}$ for $n = 25$ representative intercalation compounds, see Supplementary Table 5. These intercalation compounds are the commonly used cathodes from the Layered, Olivine, NASICON, or Spinel families, which have stable structures and large interstitial spaces for reversible ion insertion, see Fig. 5(a) [44]. We analyze the lattice geometries of $n = 25$ compounds from the X-ray diffraction data and compute their corresponding structural transformation pathways. We find that $\sim 28\%$ of the compounds undergo symmetry-lowering structural transformations during charge/discharge cycles, see Fig. 5 and Supplementary Table 5. This lattice-symmetry lowering transformation is necessary to form twin interfaces and crystallographic microstructures described in Table 1. Furthermore, we identify that intercalation compounds with Spinel and Pyrophosphate structures approximately satisfy the crystallographic design principles (i.e. form

twins, austenite/martensite microstructures) and with precise lattice-geometries can form stress-free phase transformation microstructures. Below we present our microstructural analysis using $\text{Li}_x\text{Mn}_2\text{O}_4$ as a representative compound. The analyses of other intercalation compounds are presented in the Supplementary Material.
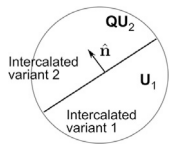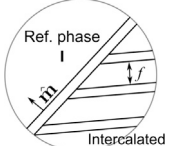
3.1.1. Twin interface

$\text{Li}_x\text{Mn}_2\text{O}_4$ (LMO) is a Spinel compound that undergoes a first-order phase transformation between LiMn_2O_4 (reference phase) and $\text{Li}_2\text{Mn}_2\text{O}_4$ (intercalated phase). Using our algorithm, we determine that the cubic-to-tetragonal structural transformation of LMO minimizes the distance function $\left\lVert \mathbf{U}^{-2} - \mathbf{I} \right\rVert^2$. This cubic ($\text{LiMn}_2\text{O}_4$) to tetragonal ($\text{Li}_2\text{Mn}_2\text{O}_4$) transformation generates three variants and their corresponding stretch tensors are listed in Table 2.[6] This transformation pathway, predicted by our algorithm, is consistent with the experimental measurements [18], and the lattice correspondence matrices determined by our code are in agreement with those in the International Tables for Crystallography [45].

Any two variants of the tetragonal-intercalated phase satisfy the compatibility condition to form a twin interface, see Table 1. Table 2 lists the twin solutions, namely vectors $\mathbf{a}$, $\hat{\mathbf{n}}$ and rotation tensors $\mathbf{Q}$, for $\mathbf{U}_2$ and $\mathbf{U}_3$ variants. We use these solutions to geometrically construct

---

[6] Variants are lattices of different orientations belonging to the same phase of the material. These variants are related to each other via a symmetry operation.

Table 2

Microstructural solutions for intercalation cathode $Li_2Mn_2O_4$. The stretch tensors $\mathbf{U}_1, \mathbf{U}_2, \mathbf{U}_3$ are computed from lattice geometry measurements reported in Ref. [18]. Using variants $\mathbf{U}_2, \mathbf{U}_3$, we construct the solutions to twin interfaces and the austenite/martensite microstructure shown in Fig. 6. The inset figures show a schematic illustration of a twin interface and an A/M interface. The vectors $\hat{\mathbf{n}}$ and $\hat{\mathbf{m}}$ denote the orientation of the twin boundary and the A/M interface, respectively, in the reference configuration.

Stretch tensor	Twin solution	A/M solution
$\mathbf{U}_1 = \begin{bmatrix} 0.9690 & 0 & 0 \\ 0 & 1.1226 & 0 \\ 0 & 0 & 0.9690 \end{bmatrix}$		
$\mathbf{U}_2 = \begin{bmatrix} 1.1226 & 0 & 0 \\ 0 & 0.9690 & 0 \\ 0 & 0 & 0.9690 \end{bmatrix}$	$\mathbf{a} = [\overline{0.2002},\ 0,\ 0.2319],\ k = -1$ $\hat{\mathbf{n}} = (0.7071,\ 0,\ \overline{0.7071})$ $K = (0.7570,\ 0,\ \overline{0.6534})$	$f = 0.2158,\ k = 1$ $\mathbf{b} = [0.0996, 0.0646, \overline{0.0043}]$ $\hat{\mathbf{m}} = (0.8653, -0.4998, -0.0376)$
$\mathbf{U}_3 = \begin{bmatrix} 0.9690 & 0 & 0 \\ 0 & 0.9690 & 0 \\ 0 & 0 & 1.1226 \end{bmatrix}$	$\mathbf{Q} = \begin{bmatrix} 0.9893 & 0 & 0.1461 \\ 0 & 1 & 0 \\ -0.1461 & 0 & 0.9893 \end{bmatrix}$	$\mathbf{Q}' = \begin{bmatrix} 0.9982 & -0.0514 & 0.0316 \\ 0.0515 & 0.9987 & -0.0006 \\ -0.0315 & 0.0022 & 0.9995 \end{bmatrix}$

the orientation of a twin interface in Fig. 6(a). The computed twin plane $K = (0.7570,\ 0,\ \overline{0.6534})$ closely matches the experimental measurement $(1, 0, 1)$ in Cartesian coordinates, see Fig. 6(a–c).

3.1.2. Austenite–martensite microstructure

The structural transformation of $Li_xMn_2O_4$ generates coherency stresses at the phase boundary between the cubic $LiMn_2O_4$ phase and the tetragonal $Li_2Mn_2O_4$ phase. To minimize these coherency stresses, the tetragonal variants form a finely twinned mixture that fits compatibly with the cubic phase and results in the characteristic austenite–martensite microstructure, see Fig. 6(c).

We use the stretch tensors $\mathbf{U}_2$ and $\mathbf{U}_3$ of $Li_xMn_2O_4$, computed in Table 2, to solve for the austenite–martensite microstructure. The stretch tensors satisfy the compatibility condition in Table 1 for a volume fraction $f = 0.2158$. Table 2 lists a solution of the austenite–martensite interface, namely vectors $\mathbf{b}$, $\hat{\mathbf{m}}$, and the rotation tensors $\mathbf{Q}'$, for corresponding volume fractions f.[7] Our analytical prediction of the volume fraction for the austenite–martensite microstructure $f = 0.2158$ is consistent with the experimental measurements of $f = 0.2$ by Erichsen et al. [18], see Fig. 6(a) and (c). Similarly, solutions to the austenite–martensite interface can be computed for other intercalation compounds that undergo symmetry-lowering transformation.
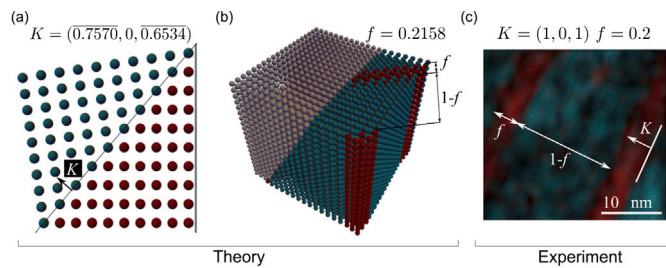

Fig. 6. Geometric construction of twin microstructures in $Li_2Mn_2O_4$. (a) Using the analytically derived twin solutions for $Li_2Mn_2O_4$ in Table 2, we geometrically construct a twin interface using variants $\mathbf{U}_2$ and $\mathbf{U}_3$. A cross-sectional view of the twin interface shows a twin-plane $K = (0.7570,\ 0,\ \overline{0.6534})$. (b) A 3D construction of the austenite/martensite interface in $Li_2Mn_2O_4$. Here, the cubic-reference phase ($LiMn_2O_4$) forms a coherent interface with finely twinned tetragonal-intercalated phase ($Li_2Mn_2O_4$). We predict the volume fraction of the twinned mixture to be $f = 0.2158$. (c) Our geometric construction closely matches the previously imaged (Bright field) LMO sample showing (101) twining plane in Cartesian coordinates and volume fraction $f = 0.2$.
Source: Reproduced with permission from American Chemical Society [18].

3.1.3. Special microstructures

We next compute stretch tensors for each intercalation compound in Supplementary Table 5 ($n = 25$) and examine whether they form special microstructures, such as the self-accommodation and the $\lambda_2 = 1$ microstructure.

From Table 1 in Methods, we recall that self-accommodation microstructures must satisfy (a) volume-preserving structural transformation, i.e., $|\det \mathbf{U} - 1| = 0$, and (b) have no relative stretching along c-axis of the lattice during transformation. Fig. 7(a) is a polar plot illustrating the volume change of intercalation compounds, $|\det \mathbf{U} - 1|$, from the geometric center at which $|\det \mathbf{U} - 1| = 0$. As can be seen in Fig. 7(a), the majority of the intercalation compounds do not preserve their volume during intercalation; but a few compounds, such as $\alpha - Li_xVOPO_4$, Li_xCrMnO_4, $Li_xMn_2O_4$, have negligible volume changes, $|\det \mathbf{U} - 1| \leq 0.05$. Although these compounds have small volume changes, they do not satisfy the remaining geometric conditions to form self-accommodating microstructures, see Supplementary Table 7. However, these compounds serve as suitable candidates that could be systematically doped to satisfy the geometric constraints for forming self-accommodating microstructures during intercalation.

From Table 1, we note that an exact interface forms between the austenite phase and one variant of the martensite phase when the middle eigenvalue is $\lambda_2 = 1$. We compute the middle eigenvalues for each intercalation compound and estimate the distance $|\lambda_2 - 1|$. Fig. 7(b) is a polar plot illustrating the radial distance of each intercalation compound from the geometric center at which $|\lambda_2 - 1| = 0$. Six of the twenty-five intercalation compounds, including $\alpha - Li_xVOPO_4$ and Li_xCrMnO_4, lie close to the geometric center with $|\lambda_2 - 1| \leq 0.1$.[8]

Overall, Figs. 7(a–b) show that none of the intercalation compounds from our representative set exactly satisfy the geometric constraints for self-accommodation and/or $\lambda_2 = 1$ condition. A few compounds (e.g., $Li_xMn_2O_4$, Li_xCrMnO_4 and $\alpha - Li_xVOPO_4$), however, approximately satisfy the geometric constraints. These materials would serve as starting compounds for first-principles calculations or topochemical synthesis that can be systematically doped to satisfy the self-accommodation and/or $\lambda_2 = 1$ conditions. We note that designing intercalation materials for the next generation of lithium batteries not only requires superior structural stability but also excellent electrochemical performance. We propose that the crystallographic design principles identified in this study must be used concurrently with other

---

[7] Following similar steps, other solutions of the austenite–martensite interface can be obtained between other tetragonal variants, see Supplementary Table 3.

[8] In addition to the $\lambda_2 = 1$ condition, we examine whether these intercalation compounds satisfy the remaining cofactor conditions necessary to form highly-reversible microstructures [28], see Supplementary Table 8. We note that none of the compounds precisely satisfy these strong compatibility conditions.
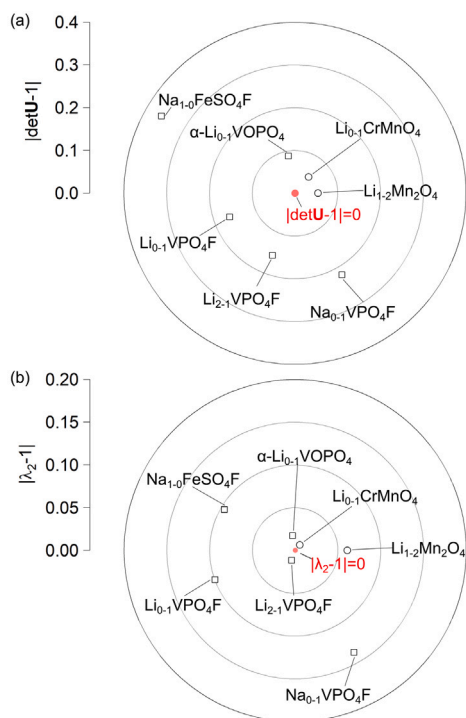
Fig. 7. (a) A polar plot illustrating the deviation of the volume changes of representative intercalation compounds from the geometric center (identified by $|\det U - 1| = 0$ condition). Please note that intercalation materials with a monoclinic reference phase are identified by "□" and with other reference phases by "○". For materials with monoclinic reference phase, the geometric center corresponds to $|\det M - 1| = 0$ [25]. (b) A polar plot illustrating the deviation of the middle eigenvalues of representative intercalation compounds from the geometric center (identified by $|\lambda_2 - 1| = 0$ condition). Please note that the angular coordinates of the data points in both subfigures (a–b) have no physical meaning, and are chosen to avoid overlap of data points.

electrochemical criteria to design novel intercalation materials with low hysteresis and high reversibility.

3.2. Study 2

We next apply our framework to analyze the structural transformations of $n = 5142$ pairs of intercalation compounds in the Materials Project database.[9] The Materials Project is an open-access database documenting the structural properties of known and computationally predicted intercalation compounds. We compute the stretch tensor for each pair of these intercalation compounds and analyze whether they undergo lattice-symmetry change during transformation and form self-accommodating and $\lambda_2 = 1$ microstructures. Finally, we compare our microstructural analysis with experimental reports on capacity retention—in particular, for electrodes that are electrochemically operated under the same conditions but have different lattice transformations. The findings from our analysis identify select candidate compounds that can be systematically doped to form shape-memory-like microstructures and show that materials nearly satisfying $|\det U - 1| \to 0$ and/or $|\lambda_2 - 1| \to 0$ have improved capacity retention.

3.2.1. Symmetry-lowering transformation

Our microstructural analysis shows that only $\sim 22\%$ ($n = 1,127$) of the known intercalation compounds undergo a lattice symmetry change during transformation, see Fig. 8(a–b). This lattice symmetry change

---

during phase transformation is necessary to generate two or more variants.[10] During phase transformation, two or more variants rotate and/or shear to form twin interfaces. These twins are characteristic features of a shape-memory-like microstructure.

Fig. 8(a) is a heat map showing the number of intercalation compounds that undergo a lattice symmetry change during transformation. We find that majority of the intercalation compounds ($n = 4,015$) do not change their lattice symmetries when transformed between the reference and intercalation phases and are concentrated at the diagonal of the heat map in Fig. 8(a). These intercalation compounds commonly undergo dilational strains that change the size of a lattice but not its symmetry. Intercalation compounds that undergo a change in lattice symmetry are located away from the diagonal of the heat map in Fig. 8(a).

Fig. 8(b) is a histogram that shows how many intercalation compounds generate two or more variants during transformation. From the $n = 1,127$ intercalation compounds undergoing symmetry-lowering transformation, nearly 50% of them generate two variants. For example, the tetragonal $\Leftrightarrow$ orthorhombic transformation in $Li_{0-1}MoO_2$ generates $N = 2$ variants. Other structural transformations, such as the cubic $\Leftrightarrow$ triclinic in $Li_{0.5-1}NiO_2$ generates $N = 24$ variants. However, these transformations, which generate multiple variants, are rare and correspond to only $\sim 1\%$ of the intercalation compounds. These compounds that generate multiple variants N during transformation have a greater number of twin solutions and would offer increased flexibility to form shape-memory-like microstructures. Overall, Figs. 8(a–b) shows that the majority of the intercalation materials do not undergo symmetry-lowering transformations and thus do not generate multiple variants. These insights help explain the absence of shape-memory-like microstructures in intercalation materials.

3.2.2. Shape-memory-like microstructures

We note that many intercalation compounds undergoing symmetry lowering transformations in Fig. 8(b) decompose into smaller products on cycling (e.g., $Mn_3CrO_8 \to CrO_2 + MnO_2$), making them unsuitable for forming shape-memory-like microstructures.[11] However, a smaller set of compounds ($n = 15$ pairs of compounds) do not decompose on intercalation and undergo displacive structural transformations. Our microstructural analysis of these select compounds identifies potential candidates that approximately satisfy the crystallographic design rules for forming self-accommodating and/or $\lambda_2 = 1$ microstructures.

Fig. 8(c) is a polar plot that shows the volume change of an intercalation compound, quantified by $|\det U - 1|$, during transformation. Intercalation compounds that form self-accommodation microstructures satisfy the crystallographic design rule $|\det U - 1| = 0$. This condition represents a zero volume change during transformation and corresponds to the geometric center of the polar plot. Fig. 8(c) shows that majority of the intercalation compounds, such as the $Cs_{0-2}WCl_6$ undergoes a large volume change $\sim 30\%$ on intercalation (i.e., $|\det U - 1| = 0.3$), and do not satisfy the condition for self-accommodation. However, select compounds, such as the $Li_{1-2}Ti_2(PO_4)_3$ from the NASICON family, $K_{0-1}Mn(PO_3)_3$ from the Phosphate family, and $Rb_2Na_{0-1}MnF_6$ from the Fluorite family have negligible volume changes with $|\det U - 1| \leq$
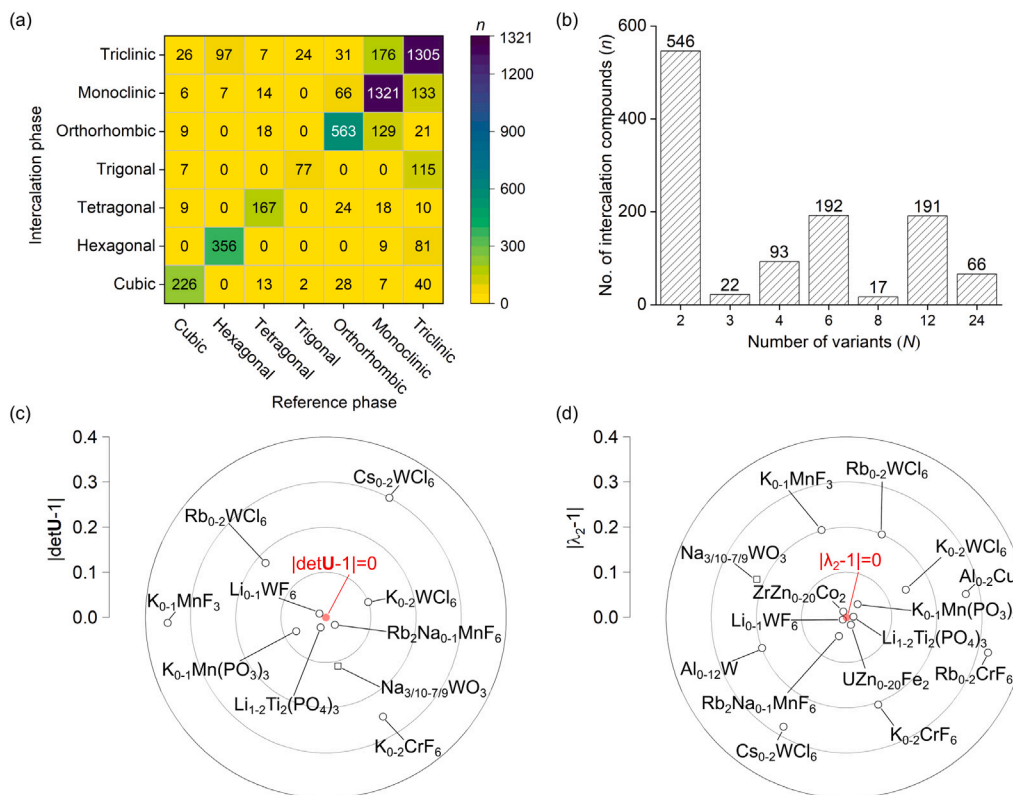

Fig. 8. (a) A heat map showing the total number of intercalation compounds n that undergo a lattice-symmetry change during intercalation. Our analysis shows that 78% of the compounds documented in the Materials Project database do not change their lattice symmetry on intercalation. These compounds are shown on the diagonal of the heat map. However, fewer than 22% of the compounds undergo a lattice-symmetry change during transformation (e.g., $n = 9$ compounds undergo cubic (reference phase) to tetragonal (intercalation phase) transformation on intercalation) and are shown at corresponding positions that are away from the diagonal. (b) A histogram of the total number of variants N generated during the phase transformation. If a compound undergoes symmetry change during phase transformation, it generates multiple $N \geq 2$ variants. Specific details to compute the number of variants are described in the Supplementary Material. Polar plots illustrating (c) the deviation of the volume changes of intercalation compounds from the geometric center (identified by $|\det \mathbf{U} - 1| = 0$ condition), and (d) the deviation of the middle eigenvalues of intercalation compounds from the geometric center (identified by $|\lambda_2 - 1| = 0$ condition). Please note that intercalation materials with a monoclinic reference phase are identified by "□" and with other reference phases by "○"; The angular coordinates of data points in (c–d) are chosen to avoid an overlap between data points.

0.07, and approximately satisfy the crystallographic design rule for self-accommodation.

Fig. 8(d) is a polar plot that shows the middle eigenvalues λ_2 of intercalation compounds during transformation. The middle eigenvalue λ_2 quantifies the relative stretch of lattices during transformation, and the crystallographic design rule $\lambda_2 = 1$ corresponds to microstructures with exactly compatible and stress-free phase-boundaries. Similar to the case in Fig. 8(c), our analysis shows that many intercalation compounds do not exactly satisfy the $\lambda_2 = 1$ condition. However, 6 out of 15 intercalation compounds, including $Li_{1-2}Ti_2(PO_4)_3$ and $K_{0-1}Mn(PO_3)_3$, lie close to the geometric center with $|\lambda_2 - 1| \leq 0.04$. This finding is in line with the emergence of $LiTi_2(PO_4)_3$ as a robust cathode coating material for solid-state batteries [48]. These results once again show that intercalation compounds in the NASICON and Phosphate families are potential candidates that can be crystallographically engineered to satisfy the geometric constraints to form $\lambda_2 = 1$ microstructures during intercalation.

Our analysis identifies several candidate intercalation compounds with lattice parameters that do not precisely satisfy the geometric constraints for self-accommodation and/or $\lambda_2 = 1$ microstructures. These compounds would serve as promising candidates that can be systematically doped (e.g., using computational DFT [22] or topochemical synthesis [24]) to exactly satisfy the $|\det \mathbf{U} - 1| = 0$ and $|\lambda_2 - 1| = 0$ conditions [50]. For example, Shin and Manthiram [23] show that the systematic doping of spinel compounds can reduce their intercalation-induced volume changes to $< 0.2\%$. Similarly, Schofield et al. [24]

showed that site-selective doping of Molybdenum in V_2O_5 electrode reduces the lattice misfit strains during phase transformation by up to 0.8% [24]. Integrating these synthesis experiments with x-ray diffraction studies (to measure lattice parameters in-situ during intercalation) further contributes to the ongoing efforts of crystallographically designing intercalation materials.

3.2.3. Comparison with experiments

We next compare our analytical results with previously published experimental literature on intercalation cathodes (Refs. [23,51,52]). Specifically, we examine the effect of geometric constraints (e.g., self-accommodation quantified by $|\det \mathbf{U} - 1|$ and stress-free phase boundaries quantified by $|\lambda_2 - 1|$) on the capacity fade of intercalation materials.

We note that the structural transformation of lattices – which at the macroscopic scale manifests as volume changes and/or stressed interfaces – leads to contact loss between active battery materials. These structural changes expose new surfaces to side reactions and hinder active-ion transport, thus contributing to capacity fade [11]. However, in batteries, capacity fade could also arise from other factors including operating conditions (e.g., C-rates, voltage window), cation dissolution, and/or electrode morphology [53]. To isolate the effect of these other factors from lattice transformations on capacity retention, we identify experiments in which authors report structural data and the cycling performance of intercalation electrodes, by holding other electro-chemo-mechanical parameters constant (e.g., Refs. [23,51,52]).
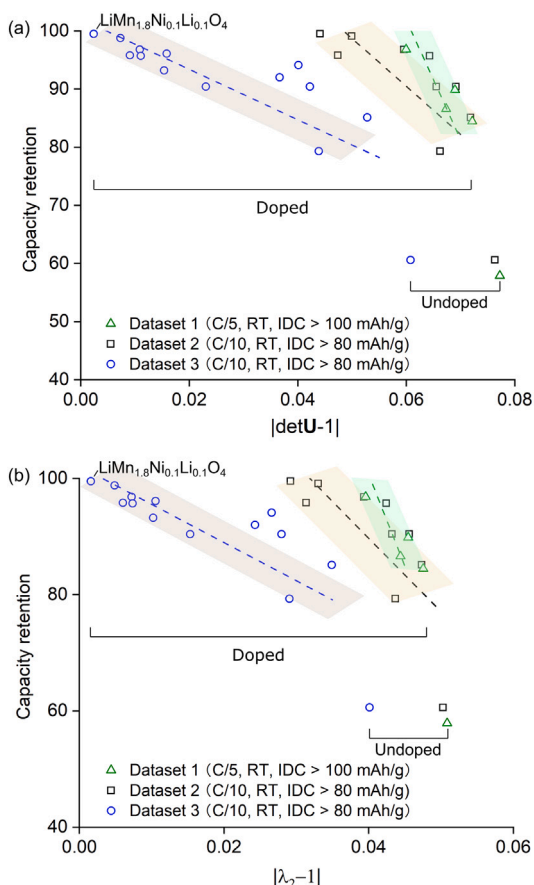
Fig. 9. Capacity retention of intercalation electrodes as a function of (a) the self-accommodation geometric constraint $|\det\mathbf{U}-1|$ and (b) the highly-reversible geometric constraint $|\lambda_2-1|$. Each electrode was cycled 50 times and under identical electrochemical conditions as indicated for each dataset. Please note RT and IDC are short for Room Temperature and Initial Discharge Capacity, respectively. Intercalation materials that closely satisfy the geometric constraints, i.e., $|\det\mathbf{U}-1| \to 0$ and $|\lambda_2-1| \to 0$ show higher capacity retention.

We select three datasets (labeled in Fig. 9 as 'Dataset 1' [51], 'Dataset 2' [52], 'Dataset 3' [23]), that contain electrodes with similar morphologies (e.g., single-phase materials, comparable particle size), and are electrochemically cycled under identical conditions (i.e., voltage window between 4.3 V and 3.5 V, Initial Discharge Capacity IDC > 80mAh/g, C/5 or C/10 rates), and at room temperatures (RT). Furthermore, the electrode particles in individual datasets are all synthesized by the same research group using solid-state reactions and are reported to have similar Mn-dissolution (see Supplementary Table 9–11 in and Refs. [23,51,52] for further details).[12]

Fig. 9(a–b) shows the capacity retention of compounds in Datasets 1–3 as a function of $|\det\mathbf{U}-1|$ and $|\lambda_2-1|$. We note that intercalation electrodes that approximately satisfy the geometric constraints $|\det\mathbf{U}-1| \to 0$ and $|\lambda_2-1| \to 0$ have greater capacity retention. For example, intercalation cathodes such as $LiMn_{1.8}Ni_{0.1}Li_{0.1}O_4$ in Dataset 3 [52] with $|\det\mathbf{U}-1| = 0.0441$ and $|\lambda_2-1| = 0.0292$ have 99.5% capacity retention even after 50 cycles. By contrast, intercalation cathodes such as the undoped $LiMn_2O_4$ in Dataset 3 with $|\det\mathbf{U}-1| = 0.0764$ and $|\lambda_2-1| = 0.0503$ in Fig. 9 only shows 60.6% capacity retention

after 50 cycles. We find similar trends in Dataset 1 [51] and Dataset 2 [23] in which doped $LiMn_2O_4$ that approximately satisfy geometric constraints have > 90% capacity retention while the capacity retention for the undoped $LiMn_2O_4$ is ∼ 60%.

Fig. 9(a–b) shows a direct correlation between capacity retention and geometric constraints $|\det\mathbf{U}-1| \to 0$ and $|\lambda_2-1| \to 0$ of intercalation materials. It is interesting to note that the two geometric constraints correspond to distinct macroscopic manifestations (i.e., zero-volume changes ($|\det\mathbf{U}-1| = 0$) and stress-free interfaces ($|\lambda_2-1| = 0$)), however, they are both conducive to improving the capacity retention. In Datasets 1–3, we are unable to determine which of the two geometric constraints has a dominant effect on capacity retention. This is a necessary limit of our work and not an intentional oversight.[13]

Overall, Fig. 9 shows that structural transformations of individual lattices, in addition to the thermodynamic and kinetic driving forces, affect the performance of intercalation materials. These results further emphasize that designing the structural transformation of individual lattices (e.g., through systematic doping), can lead to improved capacity retention and extended lifespans of electrodes. These crystallographic design criteria, however, would need to be used together with other electrochemical criteria to design suitable intercalation materials with improved performance.

4. Discussion

Our microstructural analysis shows that only a small percentage of known intercalation compounds form twins and austenite/martensite microstructures during intercalation and, a vast majority of the compounds do not satisfy the design principles for self-accommodation and/or $\lambda_2 = 1$ microstructures. This was the case in Study 1, in which selected compounds from the Spinel family form twins and austenite/martensite microstructures; however, their lattice geometries did not exactly satisfy the geometric constraints for self-accommodation and/or $\lambda_2 = 1$ microstructures. In Study 2, less than 22% of intercalation compounds reported on the Materials Project database undergo symmetry lowering transformation and thus form twins; however, none of these materials precisely satisfy the geometric constraints for self-accommodation and/or $\lambda_2 = 1$ microstructures. These compounds are promising candidates that can be systematically doped to satisfy precise lattice geometries. In the remainder of this section, we discuss some limitations of our findings, compare our results with prior work on understanding intercalation material reversibility, and present the potential impact of our work on the materials discovery program.

Two features of this work limit the conclusions we can draw from our microstructural analysis. First, we minimize a distance function $\|\mathbf{U}^{-2} - \mathbf{I}\|^2$ to identify an optimal stretch tensor $\mathbf{U}$. This distance function quantifies the total strain of a structural transformation; however, minimizing this function can generate more than one solution for the stretch tensor. In these cases, we choose the stretch tensor describing a lattice-symmetry lowering transformation as this would generate energy-minimizing microstructures. Furthermore, the accuracy of the computed structural data of intercalation compounds on the Materials Project database affects our microstructural analysis. For example, we identify candidate compounds that approximately satisfy the design constraints for self-accommodation and/or $\lambda_2 = 1$ microstructures; however, we have limited information on the chemical stability of these compounds. Many of these compounds were predicted using first-principle calculations, and rigorous experimental investigations would be necessary to ascertain their chemical stability. Second, by screening and analyzing intercalation materials using the crystallographic

---

[12] Electrodes across the different datasets differ based on the choice of substitutional dopant, particle morphologies, and operating conditions. However, in our analysis, we compare the capacity retention of electrodes within each dataset.

[13] Electrode particles in Datasets 1–3 were placed in a liquid electrolyte bath with negligible surface tractions. In the absence of surface forces both the geometric conditions $|\det\mathbf{U}-1| = 0$ and $|\lambda_2-1| = 0$ have similar conducive effects on capacity retention.

Table A.1
Summary of symbols.

Notation	Brief description
e_i	Lattice vector
$\mathbf{E} = \{\mathbf{e}_1, \mathbf{e}_2, \mathbf{e}_3\}$	Primitive unit cell spanned by $\mathbf{e}_i (i = 1, 2, 3)$
$\mathbf{E}_R, \mathbf{E}_I$	Primitive unit cell of reference and intercalated phase
$\mathbf{P}_R, \mathbf{P}_I$	Lattice correspondence matrix of reference and intercalated phase
$\mathbf{E}^A = \mathbf{E}\mathbf{P}^A$	Conventional cell related to $\mathbf{E}$ via a lattice correspondence $\mathbf{P}^A$
n	Number of intercalation compounds
N	Number of variants
$\mathbf{I}$	Identity matrix
$\mathbf{F}$	Deformation gradient tensor
$\mathbf{U}, \mathbf{U}_N$	Transformation stretch tensor. Variants $\mathbf{U}_N$ are related to each other via a symmetry operation
$\mathbf{M}$	Necessary and sufficient condition for a monoclinic compound to form self-accommodating microstructure (see Ref. [25] Section 3.4)
$\mathbf{Q}, \mathbf{Q}'$	Rotation matrices
$\mathbf{a}, \mathbf{b}, \hat{\mathbf{m}}, \hat{\mathbf{n}}$	Vectors
K	Twin plane direction
k	A constant which can take a value of ± 1
λ_i	Eigenvalues when solving $\mathbf{Q}\mathbf{U}_I - \mathbf{I} = \mathbf{b} \otimes \hat{\mathbf{m}}$
f	Volume fraction
θ	Orientation of the twin plane
$\lvert \det \mathbf{U} - 1 \rvert = 0$	Volume preservation
$\lvert \lambda_2 - 1 \rvert = 0$	Condition to form stress-free interface
p, q	Number of host-atoms in reference and intercalated unit cells
$m = \frac{p}{q}$	Ratio of host-atoms
d	Largest edge ratio
$\{a, b, c, \alpha, \beta, \gamma\}$	Lattice parameters

design principles *alone* we omit the role of other factors, such as electronic conductivity and Li diffusivity, which are important to the electrochemical performance of battery materials. The crystallographic design principles focus on one aspect – reducing the chemo-mechanical degradation of intercalation materials – that is known to accelerate electrochemical decay. We propose, however, that the crystallographic design rules identified in this work as one of the design parameters that must be used *concurrently* with other electrochemical criteria to design novel intercalation materials. With these reservations in mind, we next discuss the impact of our findings on the materials discovery program.

A key feature of our work is that we quantify the structural transformation pathways for $n > 5000$ pairs of intercalation materials using an in-house structural transformation algorithm and identify candidate compounds that can form shape-memory-like microstructures. The algorithm, unlike earlier works [33], finds an optimal structural transformation pathway (i.e., a stretch tensor that minimizes a distance function $\lVert \mathbf{U}^{-2} - \mathbf{I} \rVert^2$) between the reference and intercalated phases (as described in the Structural transformation section in Supplementary Material). Our results identify intercalation materials that approximately satisfy the design rules necessary to form self-accommodating and/or $\lambda_2 = 1$ microstructures. These compounds serve as potential candidates that can be atomically engineered (e.g., using site-selective topochemical synthesis or computational doping using DFT calculations) to satisfy precise lattice geometries. This theory-guided search for intercalation compounds would accelerate the discovery of novel intercalation materials with improved reversibility.

Another significant feature of our work is that we show a direct link between structural transformations, microstructures, and material behavior. For example, we compute the stretch tensor for $Li_{1-2}Mn_2O_4$ and quantitatively predict the microstructural features measured in Fig. 6. Furthermore, our analysis in Fig. 9 shows that, when all other electrochemical operating conditions are kept constant, intercalation compounds that nearly satisfy the self-accommodating (i.e., $\lvert \det \mathbf{U} - 1 \rvert = 0$) and $\lambda_2 = 1$ design constraints show improved ($\geq 90\%$) capacity retention. These examples demonstrate that structural transformation pathways of individual lattices, in addition to the electrochemical operating conditions and diffusion kinetics, play an important role in material performance and reversibility.

5. Conclusions

To conclude, we quantify structural transformations in intercalation compounds and identify crystallographic design rules necessary to mitigate chemo-mechanical degradation in intercalation materials. Our findings show that the majority of the known intercalation compounds are not qualified to form microstructures that are self-accommodating and/or have stress-free interfaces. However, we identify candidate intercalation compounds–such as the spinel $Li_xMn_2O_4$ and NASICON $Li_xTi_2(PO_4)_3$–that approximately satisfy the crystallographic design rules. These compounds serve as promising candidates that can be systematically doped to satisfy precise lattice geometries and thus form microstructures with minimum volume changes and/or stress-free interfaces. More generally, our analysis and the crystallographic design principles serve as a theoretical guide to discovering a new generation of intercalation materials with reduced volume changes and stress-free microstructures. These design principles will need to be used together with other electrochemical criteria to improve the overall performance of electrodes.

Declaration of competing interest

The authors declare that they have no known competing financial interests or personal relationships that could have appeared to influence the work reported in this paper.

Acknowledgments

Appendix A. Symbols and terminologies

See Tables A.1 and A.2.

Table A.2
Definition of terminology.

Terminology	Description
Deformation gradient $\mathbf{F}$	The deformation gradient $\mathbf{F}$ quantifies the deformation in continuum mechanics. It is a second-order tensor that maps line elements in the reference configuration into line elements (consisting of the same material particles) in the deformed configuration.
Stretch tensor $\mathbf{U}$	During phase transformation, the reference phase typically has a different lattice geometry from the transformed (or intercalated) phase. A stretch tensor maps a unit cells of the reference phase to the corresponding unit cell of the transformed phase. This tensor describes the local stretching (or contraction) at a material point.
Eigenvalues	A set of scalars associated with a linear system of equations. In our calculations, these values correspond to the lattice stretches during transformation.
Variant	Variants are lattices of different orientations belonging to the same phase of the material. These variants are related to each other via a symmetry operation.
Bravais lattice	A Bravais lattice is an infinite set of points in three-dimensional space generated by the translation of a single point $\mathbf{o}$ through three linearly independent lattice vectors $\mathbf{E} = \{\mathbf{e}_1, \mathbf{e}_2, \mathbf{e}_3\}$.
Primitive unit cell	The lattice vectors $\mathbf{e}_i$ enclosing the smallest repeatable volume constitute a primitive unit cell $\mathbf{E}$.
Conventional unit cell	The latter lattice vectors $\mathbf{e}_i'$ enclosing a larger volume (relative to $\mathbf{E}$) constitute a conventional unit cell $\mathbf{E}'$. A conventional cell of a crystal structure can be described in multiple ways, however, all the conventional and the primitive cells generate the same set of lattice points in 3D space.
Lattice correspondence $\mathbf{P}$	A conventional cell is related to the primitive cell via a lattice correspondence matrix $\mathbf{P}$, i.e., $\mathbf{E}' = \mathbf{E}\mathbf{P}$
Frobenius norm $\|.\|$	A matrix norm which is defined as the square root of the sum of the absolute squares of elements in a matrix. It is also equal to the square root of the matrix trace of $\mathbf{A}^{\mathrm{T}}\mathbf{A}$, i.e., $\|\mathbf{A}\| = \sqrt{\mathrm{Tr}(\mathbf{A}^{\mathrm{T}}\mathbf{A})}$

Appendix B. Supplementary data

Supplementary material related to this article can be found online at https://doi.org/10.1016/j.actamat.2023.118879.

References

[1] M. Dresselhaus, G. Dresselhaus, Intercalation compounds of graphite, Adv. Phys. 30 (2) (1981) 139–326.

[2] M.S. Whittingham, Chemistry of intercalation compounds: Metal guests in chalcogenide hosts, Prog. Solid. State Ch. 12 (1) (1978) 41–99.

[3] A.K. Padhi, K.S. Nanjundaswamy, J.B. Goodenough, Phospho-olivines as positive-electrode materials for rechargeable lithium batteries, J. Electrochem. Soc. 144 (4) (1997) 1188.

[4] X.-C. Liu, S. Zhao, X. Sun, L. Deng, X. Zou, Y. Hu, Y.-X. Wang, C.-W. Chu, J. Li, J. Wu, et al., Spontaneous self-intercalation of copper atoms into transition metal dichalcogenides, Sci. Adv. 6 (7) (2020) eaay4092.

[5] H. Zhou, et al., Two-phase transition of Li-intercalation compounds in Li-ion batteries, Mater. Today 17 (9) (2014) 451–463.

[6] J. Lim, C.-S. Yoo, Intercalation of solid hydrogen into graphite under pressures, Appl. Phys. Lett. 109 (5) (2016) 051905.

[7] N. Nadkarni, T. Zhou, D. Fraggedakis, T. Gao, M.Z. Bazant, Modeling the metal–insulator phase transition in Li_xCoO_2 for energy and information storage, Adv. Funct. Mater. 29 (40) (2019) 1902821.

[8] J.A. Lewis, J. Tippens, F.J.Q. Cortes, M.T. McDowell, Chemo-mechanical challenges in solid-state batteries, Trends Chem. 1 (9) (2019) 845–857.

[9] Y. Zhang, M. Tang, Stress-induced intercalation instability, Acta Mater. 201 (2020) 158–166.

[10] G. Chen, X. Song, T.J. Richardson, Electron microscopy study of the $LiFePO_4$ to $FePO_4$ phase transition, Electrochem. Solid-State Lett. 9 (6) (2006) A295.

[11] R. Koerver, I. Aygün, T. Leichtweiß, C. Dietrich, W. Zhang, J.O. Binder, P. Hartmann, W.G. Zeier, J. Janek, Capacity fade in solid-state batteries: interphase formation and chemomechanical processes in nickel-rich layered oxide cathodes and lithium thiophosphate solid electrolytes, Chem. Mater. 29 (13) (2017) 5574–5582.

[12] G. Bucci, B. Talamini, A.R. Balakrishna, Y.-M. Chiang, W.C. Carter, Mechanical instability of electrode-electrolyte interfaces in solid-state batteries, Phys. Rev. Mater. 2 (10) (2018) 105407.

[13] K. Xiang, W. Xing, D.B. Ravnsbæk, L. Hong, M. Tang, Z. Li, K.M. Wiaderek, O.J. Borkiewicz, K.W. Chapman, P.J. Chupas, et al., Accommodating high transformation strains in battery electrodes via the formation of nanoscale intermediate phases: operando investigation of olivine $NaFePO_4$, Nano Lett. 17 (3) (2017) 1696–1702.

[14] D. Zhang, J. Sheth, B.W. Sheldon, A.R. Balakrishna, Film strains enhance the reversible cycling of intercalation electrodes, J. Mech. Phys. Solids 155 (2021) 104551.

[15] A. Renuka Balakrishna, Crystallographic design of intercalation materials, J. Electrochem. Energy Convers. Storage 19 (4) (2022) 040802.

[16] D.A. Santos, S. Rezaei, D. Zhang, Y. Luo, B. Lin, A.R. Balakrishna, B.-X. Xu, S. Banerjee, Chemistry–mechanics–geometry coupling in positive electrode materials: a scale-bridging perspective for mitigating degradation in lithium-ion batteries through materials design, Chem. Sci. 14 (3) (2023) 458–484.

[17] C. Chu, R. James, Analysis of microstructures in Cu-14.0%Al-3.9%Ni by energy minimization, J. Phys. IV 5 (C8) (1995) C8–143.

[18] T. Erichsen, B. Pfeiffer, V. Roddatis, C.A. Volkert, Tracking the diffusion-controlled lithiation reaction of $LiMn_2O_4$ by In Situ TEM, ACS Appl. Energy Mater. 3 (6) (2020) 5405–5414.

[19] S. Rudraraju, A. Van der Ven, K. Garikipati, Mechanochemical spinodal decomposition: a phenomenological theory of phase transformations in multi-component, crystalline solids, Npj Comput. Mater. 2 (1) (2016) 1–9.

[20] D. Kim, S.-H. Kang, M. Slater, S. Rood, J.T. Vaughey, N. Karan, M. Balasubramanian, C.S. Johnson, Enabling sodium batteries using lithium-substituted sodium layered transition metal oxide cathodes, Adv. Energy Mater. 1 (3) (2011) 333–336.

[21] S. Tan, H. Xu, Observations on a CuAlNi single crystal, Contin. Mech. Thermodyn. 2 (4) (1990) 241–244.

[22] X. Zhao, Y. Tian, Z. Lun, Z. Cai, T. Chen, B. Ouyang, G. Ceder, Design principles for zero-strain li-ion cathodes, Joule 6 (7) (2022) 1654–1671.

[23] Y. Shin, A. Manthiram, Factors influencing the capacity fade of spinel lithium manganese oxides, J. Electrochem. Soc. 151 (2) (2004) A204.

[24] P. Schofield, Y. Luo, D. Zhang, W. Zaheer, D. Santos, G. Agbeworvi, J.D. Ponis, J.V. Handy, J.L. Andrews, E.J. Braham, et al., Doping-induced pre-transformation to extend solid-solution regimes in li-ion batteries, ACS Energy Lett. 7 (2022) 3286–3292.

[25] K. Bhattacharya, Self-accommodation in martensite, Arch. Ration. Mech. Anal. 120 (3) (1992) 201–244.

[26] R. Koerver, W. Zhang, L. de Biasi, S. Schweidler, A.O. Kondrakov, S. Kolling, T. Brezesinski, P. Hartmann, W.G. Zeier, J. Janek, Chemo-mechanical expansion of lithium electrode materials–on the route to mechanically optimized all-solid-state batteries, Energy Environ. Sci. 11 (8) (2018) 2142–2158.

[27] W.H. Woodford, W.C. Carter, Y.-M. Chiang, Design criteria for electrochemical shock resistant battery electrodes, Energy Environ. Sci. 5 (7) (2012) 8014–8024.

[28] X. Chen, V. Srivastava, V. Dabade, R.D. James, Study of the cofactor conditions: conditions of supercompatibility between phases, J. Mech. Phys. Solids 61 (12) (2013) 2566–2587.

[29] R. James, Z. Zhang, A way to search for multiferroic materials with "unlikely" combinations of physical properties, in: Magnetism and Structure in Functional Materials, Springer, 2005, pp. 159–175.

[30] M.D. Radin, J. Alvarado, Y.S. Meng, A. Van der Ven, Role of crystal symmetry in the reversibility of stacking-sequence changes in layered intercalation electrodes, Nano Lett. 17 (12) (2017) 7789–7795.

[31] C. Chluba, W. Ge, R. Lima de Miranda, J. Strobel, L. Kienle, E. Quandt, M. Wuttig, Ultralow-fatigue shape memory alloy films, Science 348 (6238) (2015) 1004–1007.

[32] J.M. Ball, R.D. James, Fine phase mixtures as minimizers of energy, in: Contin. Mech. Thermodyn., Springer, 1989, pp. 647–686.

[33] X. Chen, Y. Song, N. Tamura, R.D. James, Determination of the stretch tensor for structural transformations, J. Mech. Phys. Solids 93 (2016) 34–43.

[34] W. David, M. Thackeray, L. De Picciotto, J. Goodenough, Structure refinement of the spinel-related phases $Li_2Mn_2O_4$ and $Li_{0.2}Mn_2O_4$, J. Solid State Chem. 67 (2) (1987) 316–323.

[35] S. Zhou, G. Barim, B.J. Morgan, B.C. Melot, R.L. Brutchey, Influence of rotational distortions on Li^+-and Na^+-intercalation in anti-NASICON $Fe_2(MoO_4)_3$, Chem. Mater. 28 (12) (2016) 4492–4500.

[36] A. Urban, D.-H. Seo, G. Ceder, Computational understanding of Li-ion batteries, Npj Comput. Mater. 2 (1) (2016) 1–13.

[37] K. Kang, G. Ceder, Factors that affect Li mobility in layered lithium transition metal oxides, Phys. Rev. B 74 (9) (2006) 094105.

[38] A.J. Martinolich, J.J. Zak, D.N. Agyeman-Budu, S.S. Kim, N.H. Bashian, A. Irshad, S.R. Narayan, B.C. Melot, J. Nelson Weker, K.A. See, Controlling covalency and anion redox potentials through anion substitution in Li-rich chalcogenides, Chem. Mater. 33 (1) (2020) 378–391.

[39] J.L. Ericksen, On the cauchy-born rule, Math. Mech. Solids 13 (3–4) (2008) 199–220.

[40] J.C. Thomas, A.R. Natarajan, A. Van der Ven, Comparing crystal structures with symmetry and geometry, Npj Comput. Mater. 7 (1) (2021) 1–11.

[41] R.D. James, M. Wuttig, Magnetostriction of martensite, Phil. Mag. A 77 (5) (1998) 1273–1299.

[42] J. Li, R. Rogan, E. Üstündag, K. Bhattacharya, Domain switching in polycrystalline ferroelectric ceramics, Nature Mater. 4 (10) (2005) 776–781.

[43] P. Naumov, S. Chizhik, M.K. Panda, N.K. Nath, E. Boldyreva, Mechanically responsive molecular crystals, Chem. Rev. 115 (22) (2015) 12440–12490.

[44] M.S. Islam, C.A. Fisher, Lithium and sodium battery cathode materials: computational insights into voltage, diffusion and nanostructural properties, Chem. Soc. Rev. 43 (1) (2014) 185–204.

[45] T. Hahn, International Tables for Crystallography: Volume A, Space-Group Symmetry, International Union of Crystallography, 2011.

[46] A. Jain, S.P. Ong, G. Hautier, W. Chen, W.D. Richards, S. Dacek, S. Cholia, D. Gunter, D. Skinner, G. Ceder, K.a. Persson, Commentary: The materials project: A materials genome approach to accelerating materials innovation, APL Mater. 1 (1) (2013) 011002.

[47] A. Jain, G. Hautier, C.J. Moore, S.P. Ong, C.C. Fischer, T. Mueller, K.A. Persson, G. Ceder, A high-throughput infrastructure for density functional theory calculations, Comput. Mater. Sci. 50 (8) (2011) 2295–2310.

[48] Y. Xiao, L.J. Miara, Y. Wang, G. Ceder, Computational screening of cathode coatings for solid-state batteries, Joule 3 (5) (2019) 1252–1275.

[49] K. Jun, Y. Sun, Y. Xiao, Y. Zeng, R. Kim, H. Kim, L.J. Miara, D. Im, Y. Wang, G. Ceder, Lithium superionic conductors with corner-sharing frameworks, Nature Mater. (2022) 1–8.

[50] D. Zhang, A. Renuka Balakrishna, Manuscript in Preparation (2022).

[51] Y. Shin, A. Manthiram, Microstrain and capacity fade in spinel manganese oxides, Electrochem. Solid-State Lett. 5 (3) (2002) A55.

[52] Y. Shin, A. Manthiram, Influence of the lattice parameter difference between the two cubic phases formed in the 4 V region on the capacity fading of spinel manganese oxides, Chem. Mater. 15 (15) (2003) 2954–2961.

[53] T. Shi, Y.-Q. Zhang, Q. Tu, Y. Wang, M. Scott, G. Ceder, Characterization of mechanical degradation in an all-solid-state battery cathode, J. Mater. Chem. A 8 (34) (2020) 17399–17404.